Li-ion batteries of Ni-rich lithium nickel cobalt aluminium oxide coupled with high-energy lithiophilic anode

Poramane Chiochan[†], **Phansiri Suktha**[†], **Nutthaphon Phattharasupakun, Salatan Duangdangchote, Montakan Suksomboon, Worapol Tejangkura, Montree Sawangphruk**[*]

Centre of Excellence for Energy Storage Technology (CEST), Department of Chemical and Biomolecular Engineering, School of Energy Science and Engineering, Vidyasirimedhi Institute of Science and Technology, Rayong 21210 Thailand

[*]Corresponding author, e-mail: montree.s@vistec.ac.th
† These authors contributed equally to this work.

ABSTRACT: Herein, highly dispersed 10-nm lithiophilic silver nanoparticles (AgNPs) were synthesized and decorated on 3D graphene aerogel supporting materials. The prelithiated AgNPs/3D graphene aerogel exhibits a high specific capacity of 1589 mAh/g at 0.1 A/g with a high initial coulombic efficiency (ICE) of ca. 93% and a long cycling stability over 500 cycles. A Li-ion battery cell using the prelithiated AgNPs/3D graphene aerogel with a finely tuned Ag content of 0.52 at. % as the anode and the Ni-rich $LiNi_{0.88}Co_{0.09}Al_{0.03}O_2$ as the cathode exhibits a high energy density of $\sim$290 Wh/kg at 0.1 C. This new anode material may be a useful high-energy anode for next-generation Li-ion batteries.

KEYWORDS: Ni-rich Li-ion batteries, lithiophilicity, silver nanoparticles, graphene aerogel, high-energy anode

INTRODUCTION

Lithium-ion battery (LIB) is one of the best existing energy storage devices commonly used in mobile electronic devices and electric vehicles. Graphite is widely used as the anode of LIBs having a theoretical capacity of 372 mAh/g and a practical capacity of ca. 320 mAh/g, which is slightly low and not enough for next-generation high-energy LIBs. In another word, the pure graphite cannot meet huge demands of future long-range electric vehicles, which roughly need ca. 300 Wh/kg at the cell level. As a result, novel materials beyond graphite-based LIBs have been widely investigated [1]. To have high-energy batteries, our research community has been moving towards other anode materials using silicon, lithium, or lithium alloy [2]. However, there are so many issues using those materials such as the dendrite formation, dead lithium formation, poor initial coulombic efficiency (ICE), volume expansion, short life cycle, and poor safety. This is owing to their uncontrollable conversion chemistry reactions, not like the conventional intercalation chemistry of graphite.

In this work, we have investigated lithiophilic silver nanoparticles (AgNPs) decorated on three-dimensional (3D) graphene aerogel support [3] as the host of lithium. Previously, 2D graphene and heteroatom-doped graphene nanosheets and their composites were used as hosts of Li metal [4, 5]; however, the restacking issue of 2D graphene sheets by the π-π interaction limits the dispersion of Li during the plating. Many previous works also reported the enhancement of specific capacity, surface area, and pore

volume of 3D graphene compared to the conventional 2D graphene [6]. As a result, the 3D graphene is more suitable for Li metal accommodation and dendrite suppression compared to the 2D one. For further dendrite suppression, the metal nanoparticles such as Au [7], Ag [8, 9], and Si [10] were also used as lithiophilic materials. For example, the lithium plating on Ag metal forming the Li_4Ag alloy provides a theoretical capacity of 993 mAh/g [11], which is about 3-time higher than that of graphite. To enhance the alloy formation process, silver needs to be tiny nanoparticles with high dispersion. As a result, in this work, AgNPs were synthesized and dispersed on the 3D graphene aerogel supporting material, providing ultrahigh specific active surface area for the alloy formation. The 3D graphene aerogel here in this work was produced by a green microwave activation/reduction of graphene oxide [12, 13]. Furthermore, the lithiation process was used to further enhance the ICE reducing the Li loss in the SEI formation process.

On the other hand, Ni-rich cathode materials, which would be widely and commercially used in next-generation LIBs towards long-range electric vehicles (EVs) [14], were used in this work. They would replace current cathode materials such as NMC532 (AESC, Nissan Leafe), NMC622 (CATL and BYD), $LiNi_{0.8}Co_{0.15}Al_{0.05}O_2$, or NCA801505 (Panasonic, Tesla) in the next few years. To further develop Ni-rich cathode materials [15, 16], $LiNi_{0.88}Co_{0.09}Al_{0.03}O_2$ (NCA880903) was therefore used and coupled with the prelithiated AgNPs/3D rGO_{ae} anode for a full-cell configuration in this work. Interestingly, the as-fabricated battery cell prototype

here exhibits a high energy density of ∼290 Wh/kg based on active anode and cathode materials at 0.1 C. This newly designed anode material may be useful for next-generation Li-ion batteries.

MATERIALS AND METHODS

Chemicals and materials

Graphite powder (< 20 μm), polytetrafluoroethylene (60% dispersion in H_2O), potassium chloride (⩾ 99.99%), and polyvinylidene fluoride (Mw∼534 000) were from Sigma-Aldrich (MA, USA). Sulfuric acid (98%), nitric acid (65%), n-methyl-2-pyrrolidone (99.5%), hydrochloric acid (37%), ethylene glycol (99.5%), and ethanol (99%) were from QRec (Auckland, New Zealand). Hydrogen peroxide (30%) was from Chem Supply (Gillman, Australia). Carbon black (99%), lithium nickel cobalt aluminium oxide ($LiNi_{0.88}Co_{0.09}Al_{0.03}O_2$ or NCA880903) powder, copper (Cu) foam (280 g/m^2), aluminium (Al) foil (thickness∼18 μm) lithium chip, polyethylene (PE) film (thickness∼25 μm), lithium hexafluorophosphate ($LiPF_6$) in a mixture of ethylene carbonate (EC), and dimethyl carbonate (DMC) were from Gelon (Shandong, China). Sodium nitrate (99%) and potassium hexacyanoferrate (II) trihydrate (⩾ 99.99%) were from Ajax Finechem (New South Wales, Australia). Potassium permanganate (99%) was from UNIVAR (Seattle, USA). All chemicals were used without further purification. Deionized water was from Millipore system (DI water, 15 MΩ cm).

Synthesis of 3D rGO$_{ae}$

For the synthesis of graphene oxide (GO), 5.0 g of graphite powder and 7.5 g of sodium nitrate were mixed in 500 ml of concentrated sulfuric acid in an ice-bath at the temperature below 20 °C. Then, 40 g of potassium permanganate was slowly added into the mixture and stirred for 24 h at an ambient temperature. Five hundred ml of deionized water and 150 ml of hydrogen peroxide were subsequently added into the mixture and kept stirring for 24 h. The mixture was washed with 5% hydrochloric acid and then centrifuged with deionized water for several times until neutral [17]. The obtained product was later freeze-dried for 72 h. Finally, the 3D rGO$_{ae}$ was synthesized by the microwave method at 250 W using the GO precursor [13].

Synthesis of 3D rGO$_{ae}$/Ag composite

For the synthesis of 3D rGO$_{ae}$/Ag composite, 10 mg of rGO$_{ae}$ powder was added into 10 ml of ethylene glycol as a reducing agent and solvent and then heated up to 80 °C. Then, silver nitrate was added into the mixture and stirred for 30 min at 80 °C. The amount of $AgNO_3$ for 10, 50, and 100 mM are 17, 85, and 170 mg, respectively. The composite was washed using ethanol and deionized water for three times. Finally,

the 3D rGO$_{ae}$/Ag composite was dried at 80 °C in an oven overnight.

Fabrication of the electrode

For the electrochemical test, the electrode was prepared by mixing the active material with carbon black and PVDF binder at a weight ratio of 8:1:1, where NMP was used as the dissolving solvent. The 1 μl of suspension was then dropped onto the glassy carbon electrode (GCE) as the working electrode. For lithium-ion batteries (LIBs), the active material, carbon black, and PTFE binder at a weight ratio of 8:1:1 were mixed in ethanol using an agate mortar. The mixture was rolled to sheet and then pressed on the copper foam current collector with a diameter of 1.58 cm. The electrode was dried for 24 h in 120 °C in oven. For the preparation of NCA880903 cathode, active material, carbon black, and PVDF binder at a weight ratio of 8:1:1 were mixed in NMP solvent using an agate mortar and pestle. The slurry mixture was coated on the Al foil current collector by a doctor blade coating and then dried at 120 °C in oven for 24 h. After pressing, the NCA880903 electrode was cut into the circle with a diameter of 1.58 cm.

Characterizations

The morphology of as-synthesized materials and electrodes was characterized by Field-emission scanning electron microscopy (FE-SEM, JEOL JSM-7610F, Tokyo, Japan) and transmission electron microscopy (TEM, Hitachi HT7700, IL, USA). The structural property was characterized by using X-ray diffraction (XRD, Bruker D8 advance with Cu Kα radiation, λ = 1.54056 Å, MA, USA). The chemical structure was characterized by Fourier transform infrared spectroscopy (FTIR, PerkinElmer, MA, USA) and Raman spectroscopy (Bruker, excitation wavelength 532 nm, MA, USA). The specific surface area and pore volume were measured by nitrogen adsorption/desorption (3Flex-physisorption, Micromeritics, Norcross, USA) with the Brunauer-Emmett-Teller (BET) and Barrett-Joyner-Halenda (BJH) methods, respectively. The chemical composition was analyzed by X-ray photoelectron spectroscopy (XPS, JEOL, JSP-9010MC, Tokyo, Japan).

For the electrochemical test of the half-cell system, the active material on the GCE, platinum rod, and Ag/AgCl (3 M KCl) were used as working, counter, and reference electrodes, respectively. Then, the electrochemical active surface area (EASA) and the heterogeneous rate constant ($k°$) were tested by cyclic voltammetry (CV) and electrochemical impedance spectroscopy (EIS), respectively, in 6 mM $Fe(CN)_6^{4-}$ in 0.1 M KCl solution using AUTOLAB potentiostat (PGSTAT302N, Metrohm, Herisau, Switzerland) with NOVA 1.11 software.

For the electrochemical characterization of LIBs,

the half-cell was assembled into a coin cell 2032 type with lithium chip (Li chip) as counter and reference electrodes and polyethylene (PE) film (thickness~25 μm, Gelon) as a separator. The electrolyte is 1.0 M Lithium hexafluorophosphate (LiPF$_6$) in a mixture of ethylene carbonate (EC) and dimethyl carbonate (DMC) 1:1 by volume. The half-cell was fabricated in an argon-filled glove box. For the prelithiation process, the anode electrode was placed on a glass slide. The electrolyte was dropped on the electrode, and then Li chip was directly attached on the electrode. Another glass slide was covered and pressed by two metal paper binder clips for 3 h. The full cell was assembled using the prelithiated anode, the NCA880903 cathode, and the PE separator. The CV and EIS of full LIB cells were tested by using AUTOLAB potentiostat (PGSTAT302N, Metrohm) with NOVA 1.11 software. The galvanostatic charge/discharge was tested by using a battery tester (Neware, Gelon).

RESULTS AND DISCUSSION

Physicochemical properties

The morphology of 3D rGO$_{ae}$ and 3D rGO$_{ae}$/Ag composites was investigated using FE-SEM and TEM (Fig. 1). Fig. 1a and b show FE-SEM and TEM images of 3D rGO$_{ae}$ prepared by a green microwave reduction method at 250 W [13]. It shows a 3D networking structure with interconnected graphene sheets. The FE-SEM images of 3D rGO$_{ae}$/Ag composites synthesized by mixing the 3D rGO$_{ae}$ and silver nitrate (AgNO$_3$) at different concentrations in ethylene glycol at 80 °C for 30 min are shown in Fig. 1(c,e,g). The Ag atomic percent (Ag at. %) was examined by X-ray photoelectron spectroscopy (XPS). The samples were denoted as 3D rGO$_{ae}$/Ag$_{Ag\%}$ including 3D rGO$_{ae}$/Ag$_{0.52}$, 3D rGO$_{ae}$/Ag$_{0.72}$, and 3D rGO$_{ae}$/Ag$_{0.81}$ initially synthesized using AgNO$_3$ precursors at 10, 50, and 100 mM, respectively. For 3D rGO$_{ae}$/Ag$_{0.72}$ (Fig. 1e) and 3D rGO$_{ae}$/Ag$_{0.81}$ (Fig. 1g), the AgNPs are observed on the rGO surface. For TEM images, AgNPs are clearly decorated on the 3D rGO$_{ae}$ nanosheets (Fig. 1(d,f,h)) as compared to TEM image of 3D rGO (Fig. 1b). The diameter of AgNPs is ~5–10 nm for 3D rGO$_{ae}$/Ag$_{0.52}$ (Fig. 1d). By increasing AgNO3 precursor contents at the synthesis process, the particle sizes of AgNPs are increased to 10–20 nm for 3D rGO$_{ae}$/Ag$_{0.72}$ and 20–100 nm for 3D rGO$_{ae}$/Ag$_{0.81}$ (Fig. 1f and 1h), respectively.

The XRD patterns of 3D rGO$_{ae}$ and 3D rGO$_{ae}$/Ag composites are shown in Fig. 2a. The 3D rGO$_{ae}$ shows two broad peaks at 2θ values of 29° and 44° [18]. The diffraction peak (002) at a 2θ value of 29° is the characteristics of graphene [19], whilst the 3D rGO$_{ae}$/Ag composites show (002) peaks shifted to 2θ values of 23–25°. Also, the 3D rGO$_{ae}$/Ag composites show the diffraction peaks at 2θ values of 38.3°, 44.6°, 64.7°, and 77.6°, which can be assigned to the (111),

Table 1 Elements found in 3D rGO$_{ae}$/AgNPs samples at different Ag contents determined by XPS.

Sample	C (at. %)	O (at. %)	Ag (at. %)	S (at. %)
3D rGO$_{ae}$	91.50	7.70	–	0.79
3D rGO$_{ae}$/Ag$_{0.52}$	89.89	8.27	0.52	1.29
3D rGO$_{ae}$/Ag$_{0.72}$	92.31	5.56	0.72	1.39
3D rGO$_{ae}$/Ag$_{0.81}$	92.34	5.46	0.81	1.36

(200), (220), and (331) planes of silver, respectively, and 2θ value of 34.5° which is a characteristic peak of AgO [20]. Fig. 2b shows Raman spectra of 3D rGO$_{ae}$ and 3D rGO$_{ae}$/Ag composites. This result shows that D, G, 2D, and D+G bands are at around 1362, 1604, 2697, 2956 cm^{-1}, respectively. D and G bands correspond to the disorder structure or defect (sp^3) and the ordered structure (sp^2) of graphitic sheet. The I$_D$/I$_G$ ratio of 3D rGO$_{ae}$ is 0.82, while the 3D rGO$_{ae}$/Ag composites show higher intensity ratio of D to G band (I$_D$/I$_G$ = 0.96 of 3D rGO$_{ae}$/Ag$_{0.52}$, I$_D$/I$_G$ = 0.96 of 3D rGO$_{ae}$/Ag$_{0.72}$, and I$_D$/I$_G$ = 1.02 of 3D rGO$_{ae}$/Ag$_{0.81}$). In addition, two peaks at ~663 and 1024 cm^{-1} are Ag—O and Ag bands, respectively, corresponding to the XRD result. The FTIR spectra (Fig. 2c) show four peaks at ~1048, 1280, 2938, and 3298 cm^{-1}, which are C—O, C—O—C, C—H, and —OH stretching modes, respectively. (Fig. 2d) reveals N$_2$ gas adsorption/desorption isotherms of 3D rGO$_{ae}$ and 3D rGO$_{ae}$/Ag composites, which are in a type-IV isotherm [21]. The 3D rGO$_{ae}$ shows a BET surface area of 640 m^2/g and a pore volume of 3.74 cm^3/g, which is great for the supporting material, whilst those two properties of 3D rGO$_{ae}$/Ag composites are decreased as a function of Ag content (589 m^2/g and 1.80 cm^3/g for 3D rGO$_{ae}$/Ag$_{0.52}$, 478 m^2/g and 1.13 cm^3/g for 3D rGO$_{ae}$/Ag$_{0.72}$, and 465 m^2/g and 1.19 cm^3/g for 3D rGO$_{ae}$/Ag$_{0.81}$), indicating the occupied space by AgNPs.

Surface chemistry analysis

XPS survey spectra (Fig. 3a) reveal all elements of 3D rGO$_{ae}$ and 3D rGO$_{ae}$/Ag composites. Ag element is clearly found for the 3D rGO$_{ae}$/Ag composites. The quantitatively elemental content of all samples is listed in Table 1. The C1s XPS spectra of 3D rGO$_{ae}$ and 3D rGO$_{ae}$/Ag composites (Fig. 3b-e) show three deconvoluted peaks including C—C (284.7 eV), C—O (285.7 eV), and C=O (288.5 eV) [22, 23]. Fig. 3f shows the narrow-scan Ag3d spectrum of 3D rGO$_{ae}$/Ag$_{0.52}$. Two peaks at 368.4 and 374.4 eV indicate metallic silver (Ag^0), and other peaks at 367.0 and 373.0 eV are owing to silver oxide. The Ag3d narrow scans of 3D rGO$_{ae}$/Ag$_{0.72}$ and 3D rGO$_{ae}$/Ag$_{0.81}$ are also shown in Fig. 3g and 3h, respectively.
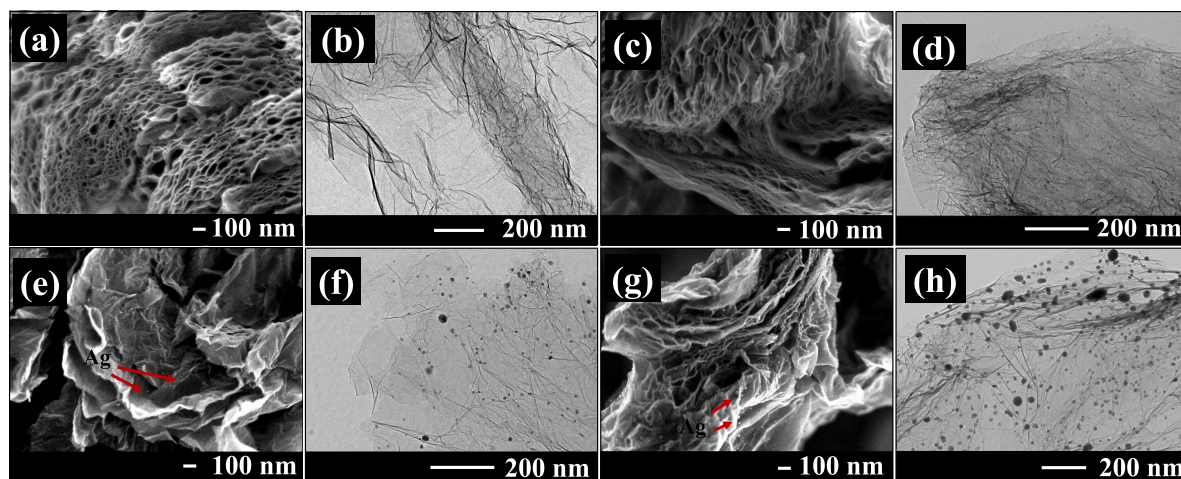
Fig. 1 FE-SEM (left) and TEM (right) images of 3D rGO$_{ae}$/Ag samples at different Ag contents; (a,b) 3D rGO$_{ae}$, (c,d) 3D rGO$_{ae}$/Ag$_{0.52}$, (e,f) 3D rGO$_{ae}$/Ag$_{0.72}$, and (g,h) 3D rGO$_{ae}$/Ag$_{0.81}$.

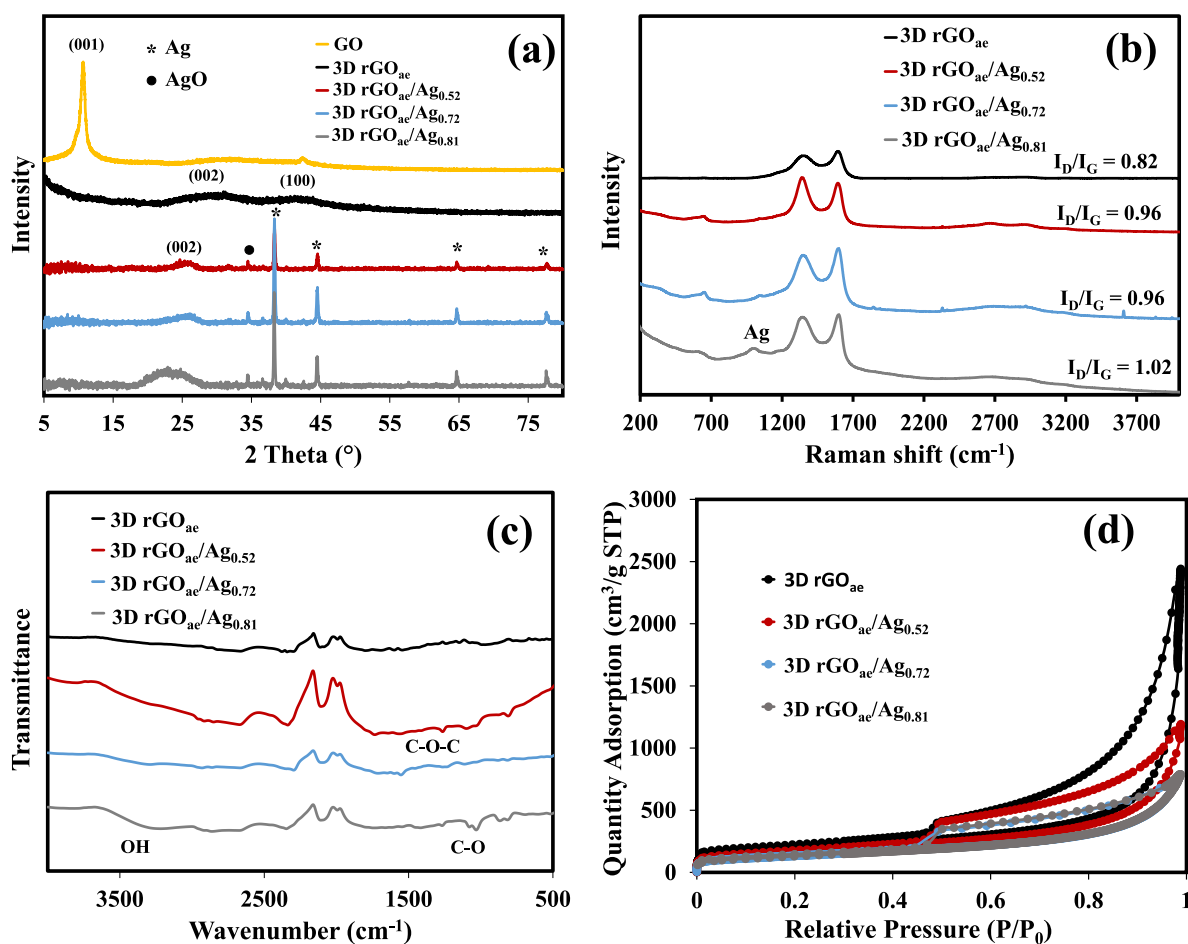**Fig. 2** (a) XRD patterns, (b) Raman spectra, (c) FTIR spectra, and (d) Nitrogen adsorption/desorption isotherm of 3D rGO$_{ae}$/Ag with different Ag contents.
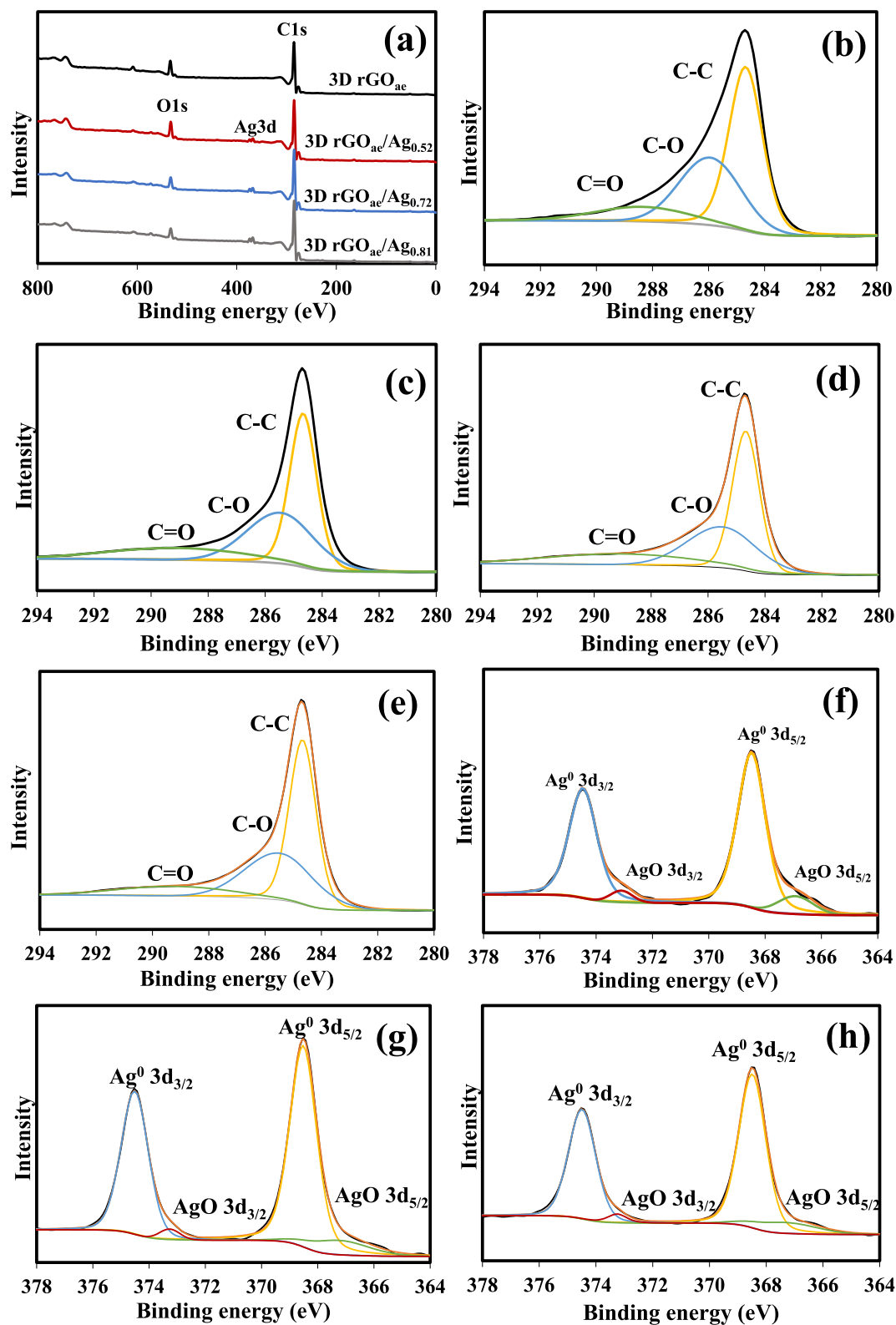
Fig. 3 XPS results including (a) wide-scan spectra of 3D rGO$_{ae}$/Ag at different Ag contents, narrow-scan C1s spectra of (b) 3D rGO$_{ae}$, (c) 3D rGO$_{ae}$/Ag$_{0.52}$, (d) 3D rGO$_{ae}$/Ag$_{0.72}$, (e) 3D rGO$_{ae}$/Ag$_{0.81}$ as well as narrow-scan Ag3d spectra of (f) 3D rGO$_{ae}$/Ag$_{0.52}$, (g) 3D rGO$_{ae}$/Ag$_{0.72}$, and (h) 3D rGO$_{ae}$/Ag$_{0.81}$.
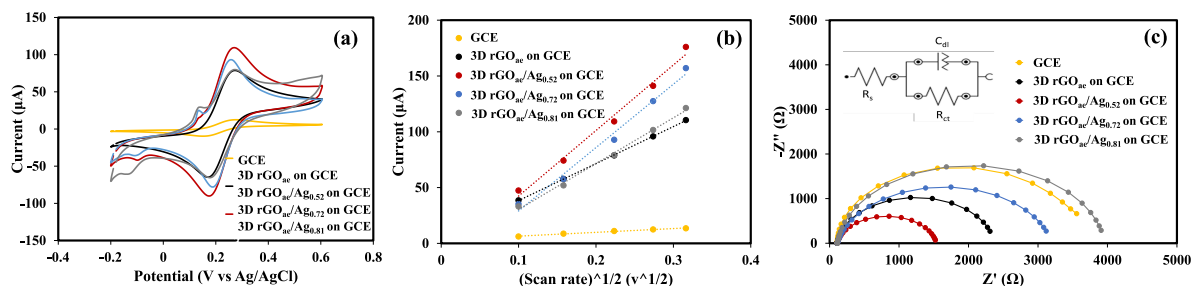
Fig. 4 (a) Cyclic voltammograms of modified electrodes at a scan rate of 0.05 V/s, (b) the relationship between the square root of scan rate and anodic current, and (c) Nyquist plot of modified electrodes in 6 mM $Fe(CN)_6^{4-}$ in 0.1 M KCl.

Electrochemical evaluation

The electrochemical property of highly dispersed Ag-NPs decorated on the 3D rGO_{ae} surface was tested in a redox mediator solution ($Fe(CN)_6^{4-}$) using cyclic voltammetry (CV) and electrochemical impedance spectroscopy (EIS). For CV, Fig. 4a reveals the pair-well peak of $Fe(CN)_6^{4-}$ at ~0.24 V (anodic potential, E_{pa}) and 0.18 V (cathodic potential, E_{pc}) at all electrodes. The potential differences (ΔE) of all electrodes are 0.111, 0.104, 0.097, 0.083, and 0.099 V for glassy carbon electrode (GCE) or the control electrode, 3D rGO_{ae}, 3D $rGO_{ae}/Ag_{0.52}$, 3D $rGO_{ae}/Ag_{0.72}$, and 3D $rGO_{ae}/Ag_{0.81}$, respectively, which are higher than 0.059 V indicating a quasi-reversible $Fe(CN)_6^{4-}/Fe(CN)_6^{3-}$ reaction. Interestingly, the AgNPs decorated on 3D rGO_{ae} surfaces lead to two small peaks on the CV at 0.13 V vs. Ag/AgCl, which is the oxidation or stripping of Ag, and at −0.1 V vs. Ag/AgCl, which is the reduction of silver ions. AgNPs are oxidized and stable at AgO structure, which is in good agreement with the XPS result. The anodic peak current (I_{pa}) and catholic peak current (I_{pc}) of AgNPs decorated 3D rGO_{ae} samples increase as compared with those of the pristine 3D rGO_{ae} material and GCE, indicating their high electrochemical activity. Also, the CVs show the increasing current as a function of increasing scan rate (see in Fig. 4b), indicating the diffusion limit. The electrochemical active surface area (EASA) of all samples was also determined by the Randle Sevcik equation (Eq. (1)) [24, 25]:

$$i_p = 2.69 \times 10^5 n^{3/2} A D_s^{1/2} C_s \nu^{1/2} \qquad (1)$$

where i_p is the peak current (A), n is the number of electrons transferred in the redox reaction ($n = 1$), A is the EASA of the electrode (cm²), D_s is the diffusion coefficient of $Fe(CN)_6^{4-}$ in KCl (7.4×10^{-6} cm²/s) [25], C_s is the concentration of the $Fe(CN)_6^{4-}$ (mol/cm³), and ν is the scan rate (V/s). The EASA values of bare GCE, 3D rGO_{ae}, 3D $rGO_{ae}/Ag_{0.52}$, 3D $rGO_{ae}/Ag_{0.72}$, and 3D $rGO_{ae}/Ag_{0.81}$ are found to be ca. 0.008, 0.075, 0.133, 0.129, and 0.093 cm², respectively. To further study the heterogeneous rate constant of electron transfer ($k°$, cm/s) at the electrode-electrolyte interface, the

EIS was carried out at 2000 rpm to overcome the diffusion limit. The corresponding equivalent circuit was fitted as an inset image in Fig. 4c. It was found that the semi-circle from the Nyquist plot of the 3D $rGO_{ae}/Ag_{0.52}$ indicates the charge transfer resistance (R_{ct}) of 1.43 KΩ, which shows lower resistance than 3D rGO_{ae} with the R_{ct} of 2.26 KΩ, 3D $rGO_{ae}/Ag_{0.72}$ with the R_{ct} of 3.09 KΩ, bare GCE with the R_{ct} of 3.33 KΩ, and 3D $rGO_{ae}/Ag_{0.81}$ with the R_{ct} of 3.85 KΩ. The $k°$ value was calculated using Eq. (2) as follows [25]:

$$R_{ct} = \frac{RT}{nF^2 A k° C_s} \qquad (2)$$

where R is the gas constant, T is the absolute temperature, and A is the surface area of the working electrode. The enhanced $k°$ of 3D $rGO_{ae}/Ag_{0.52}$ (4.4×10^{-4} cm/s) was revealed to be ca. ~1.6, ~2.0, and ~2.8 times higher than that of 3D rGO_{ae} (2.8×10^{-4} cm/s), 3D $rGO_{ae}/Ag_{0.72}$ (2.0×10^{-4} cm/s), and 3D $rGO_{ae}/Ag_{0.81}$ (1.6×10^{-4} cm/s), respectively.

Electrochemical evaluation of the half-cell electrode

To investigate the electrochemical performance of the as-prepared materials, CV and galvanostatic charge-discharge (GCD) were systematically carried out. Fig. 5a and 5b display CVs of 3D $rGO_{ae}/Ag_{0.52}$ and 3D rGO_{ae} electrodes, respectively, at a scan rate of 0.1 mV/s in a working potential range of 0.0–3.0 V (vs. Li/Li⁺). The reduction peak at ~0 V and the oxidation peak at ~0.29 V vs. Li/Li⁺ are due to the electroplating and stripping of lithium into the as-prepared materials, respectively. At the 1st cycle, the reduction peak at ~0.6 V vs. Li/Li⁺ shows the SEI formation due to the reaction between Li electrode and the electrolyte [19]. Fig. 5c shows GCDs at the 1st cycle of 3D rGO_{ae} and 3D rGO_{ae}/Ag composites for which in the discharge step at 0.1 A/g, the plateaus can be observed at ca. 0.6 V vs. Li/Li⁺, indicating the SEI formation on the 3D rGO_{ae} surface, which is in good agreement with the CV result. The rate capabilities of 3D rGO_{ae} and 3D rGO_{ae}/Ag electrodes are also shown in Fig. 5d. Both 3D rGO_{ae} and 3D $rGO_{ae}/Ag_{0.52}$ electrodes show higher capacity
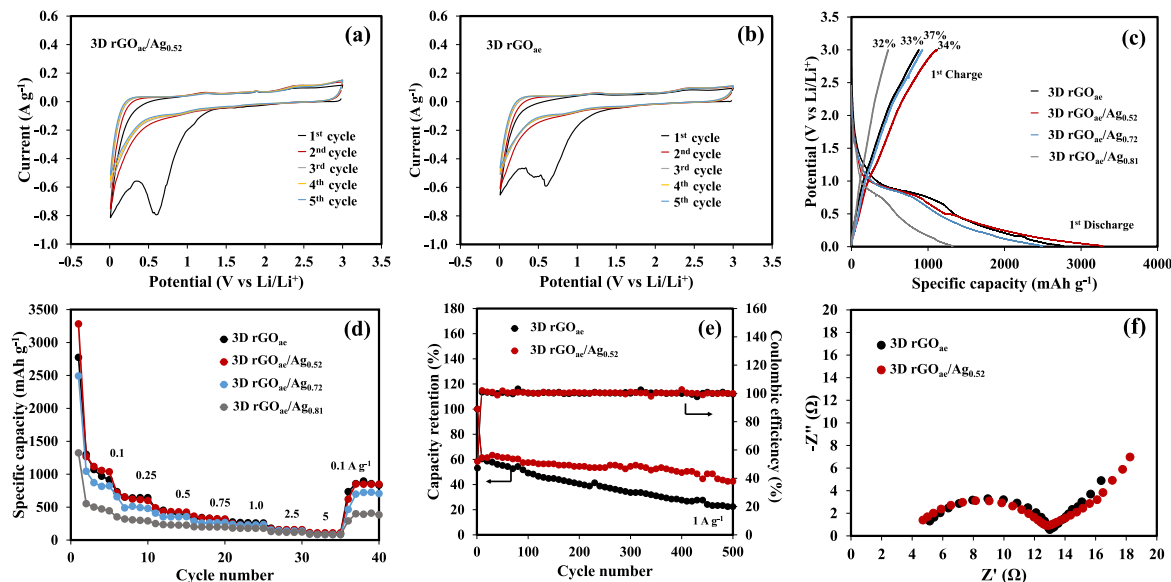
Fig. 5 (a) CVs of 3D rGO$_{ae}$/Ag$_{0.52}$, (b) CV curves of 3D rGO$_{ae}$, (c) GCDs at the initial cycle, (d) Rate capabilities at 0.1 to 5.0 A/g of 3D rGO$_{ae}$/Ag at different Ag contents, (e) cycling stability of 3D rGO$_{ae}$ and 3D rGO$_{ae}$/Ag$_{0.52}$ at a current density of 1 A/g, and (f) Nyquist plot of unprelithiated 3D rGO$_{ae}$ and 3D rGO$_{ae}$/Ag$_{0.52}$.
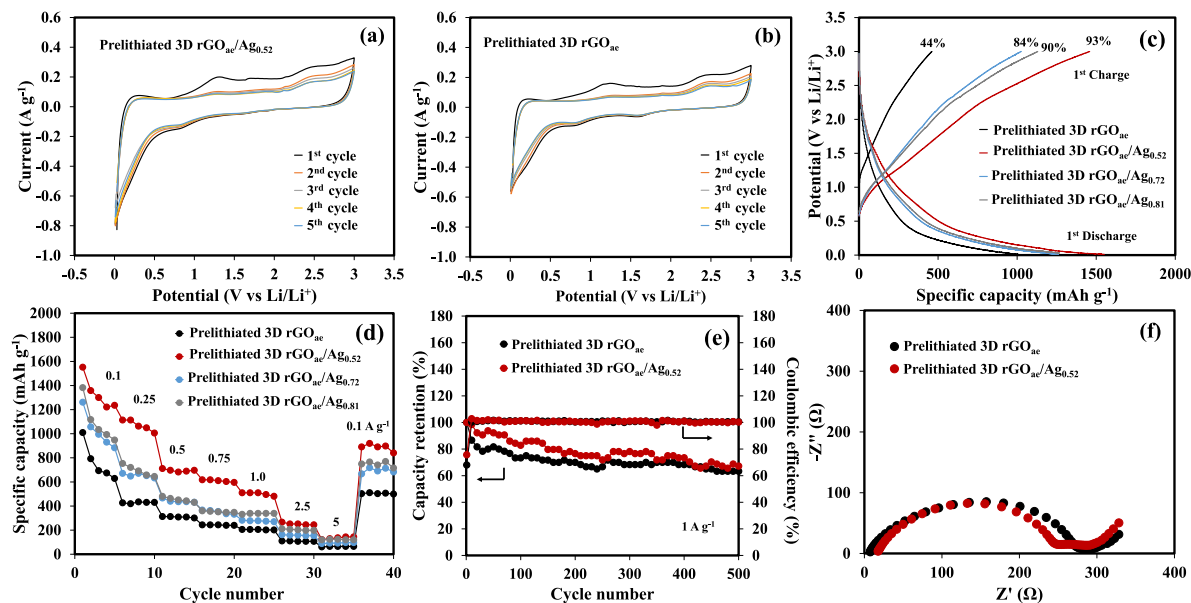

Fig. 6 (a) CVs of prelithiated 3D rGO$_{ae}$/Ag$_{0.52}$, (b) CVs of prelithiated 3D rGO$_{ae}$, (c) GCDs at the initial cycle, (d) Rate capabilities at 0.1 to 5.0 A/g of prelithiated 3D rGO$_{ae}$/Ag at different Ag contents, (e) cycling stability of prelithiated 3D rGO$_{ae}$ and 3D rGO$_{ae}$/Ag$_{0.52}$ at a current density of 1 A/g, and (f) Nyquist plot of prelithiated 3D rGO$_{ae}$ and 3D rGO$_{ae}$/Ag$_{0.52}$.

than 3D rGO$_{ae}$/Ag$_{0.72}$ and 3D rGO$_{ae}$/Ag$_{0.81}$ electrodes at low current density. Fig. 5e shows the cycling performance of 3D rGO$_{ae}$ and 3D rGO$_{ae}$/Ag$_{0.52}$ electrodes after 500 cycles for which the capacity retention of 3D rGO$_{ae}$/Ag$_{0.52}$ electrode is much higher than that of the bare 3D rGO$_{ae}$. Fig. 5f shows the Nyquist plot of 3D rGO$_{ae}$ and 3D rGO$_{ae}$/Ag$_{0.52}$ electrodes, indicat-

ing that the semi-circle diameter of 3D rGO$_{ae}$/Ag$_{0.52}$ electrode is like that of 3D rGO$_{ae}$ electrode (∼8 Ω). However, the ICE values of all electrodes are rather low, only 32–37%, and thus the prelithiation process was necessarily employed. The results are shown in Fig. 6. The reduction peak due to the SEI formation of the prelithiated electrodes was not observed
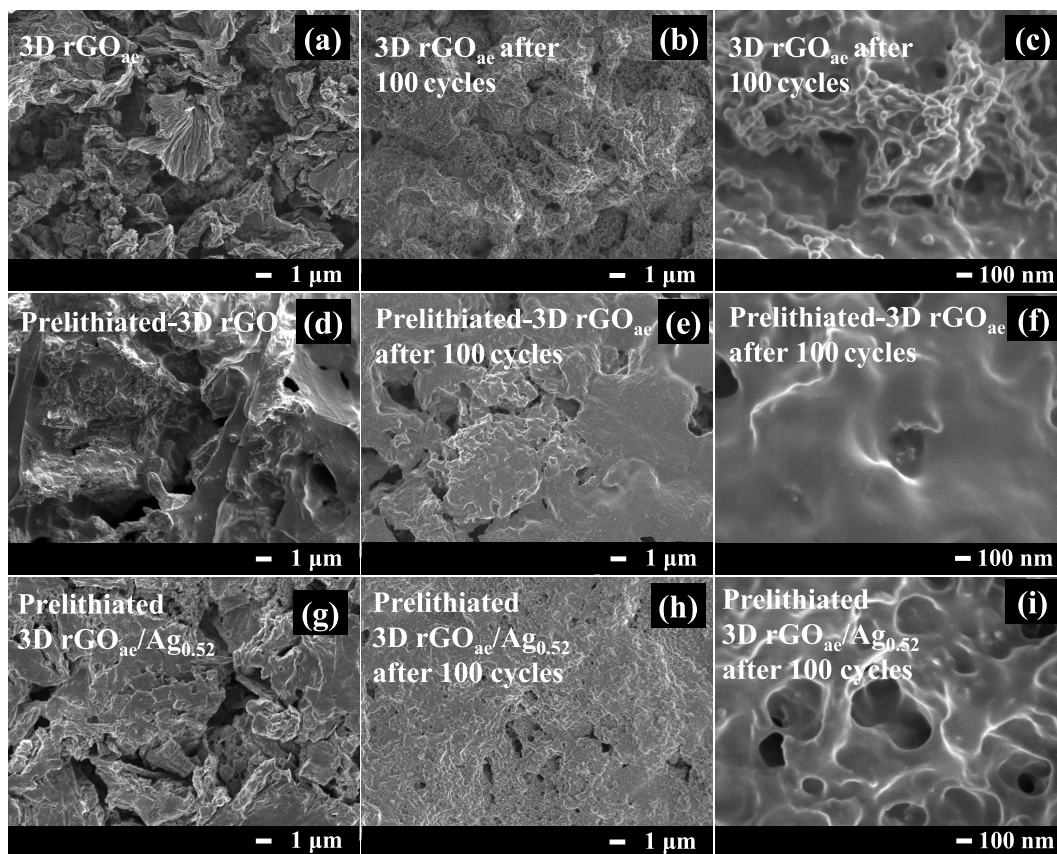
Fig. 7 FE-SEM images of (a) 3D rGO$_{ae}$, (b,c) 3D rGO$_{ae}$ after charged/discharged for 100 cycles, (d) prelithiated 3D rGO$_{ae}$, (e,f) prelithiated 3D rGO$_{ae}$ after charged/discharged for 100 cycles, (g) prelithiated 3D rGO$_{ae}$/Ag$_{0.52}$, and (h,i) prelithiated 3D rGO$_{ae}$/Ag$_{0.52}$ after charged/discharged for 100 cycles.
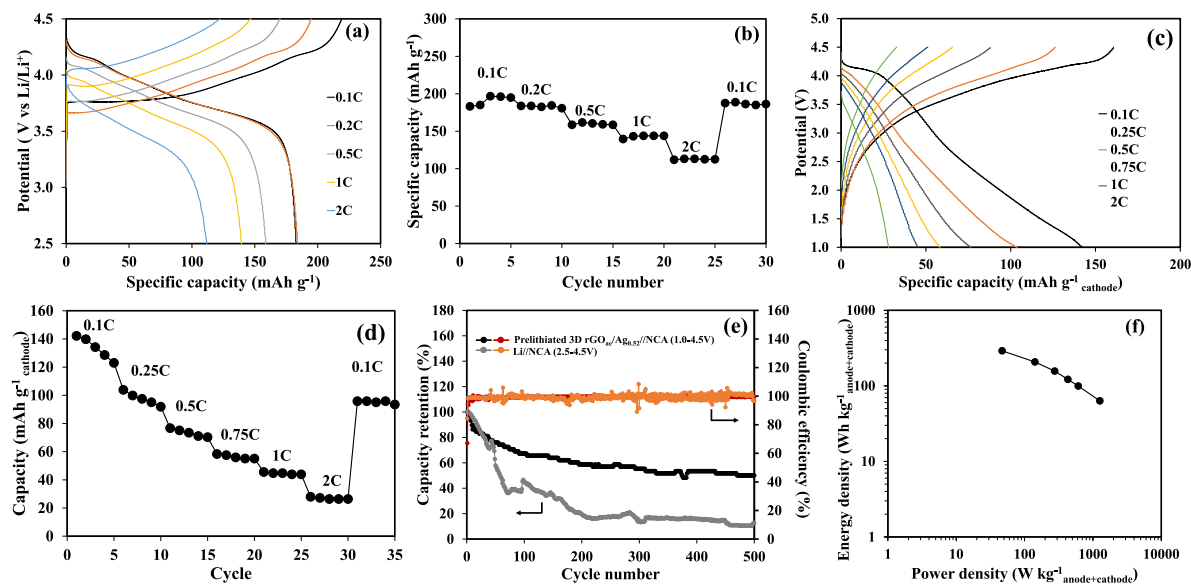

Fig. 8 Electrochemical property of NCA880903 half-cell electrode; (a) GCD curves at initial cycle, (b) Rate capabilities at 0.1 C to 2 C as well as electrochemical performance of the prelithiated 3D rGO$_{ae}$/Ag$_{0.52}$/NCA880903 full cell, (c) GCD curves at initial cycle, (d) Rate capabilities at 0.1 C to 2 C, (e) Cycling stability at 1 C, and (f) Ragone plot based on a total active mass including anode and cathode materials.

in Fig. 6a and 6b, indicating the stable prelithiated anode. This is a major advantage of the prelithiation process. Fig. 6c shows the GCD profiles at the 1st cycle of all prelithiated electrodes. This result indicates that the ICE is rather high. Especially, the prelithiated 3D $rGO_{ae}/Ag_{0.52}$ shows the highest ICE of 93% with a low initial irreversible capacity loss of 93 mAh/g. Fig. 6d shows the rate capability of prelithiated 3D rGO_{ae}/Ag at different Ag contents. Again, the prelithiated 3D $rGO_{ae}/Ag_{0.52}$ exhibits the highest specific capacity of 840 mAh/g at a current density of 1 A/g after 40 cycles, whilst the specific capacity of prelithiated 3D rGO_{ae} without Ag is only 500 mAh/g after 40 cycles. The cycling performances of prelithiated 3D rGO_{ae} and 3D $rGO_{ae}/Ag_{0.52}$ electrodes after 500 cycles are shown in Fig. 6e. Clearly, the capacity retention of prelithiated electrode is much higher than that of non-prelithiated one. This result shows that the prelithiation process can enhance the cycling stability. The Nyquist plots of prelithiated 3D rGO_{ae} and 3D $rGO_{ae}/Ag_{0.52}$ electrodes (Fig. 6f) display the smaller semicircle diameter or the R_{ct} indicating fast charge transfers.

Post-mortem analysis

The improved performance of the prelithiated electrode was confirmed via FE-SEM images over 100 cycles (Fig. 7). This result shows the smooth surface of the prelithiated electrode without lithium dendrite and dead lithium, whilst the 3D rGO_{ae} electrode without both AgNPs and the prelithiation process exhibits the lithium dendrites on its surface. The Li-ion full cell using the prelithiated 3D $rGO_{ae}/Ag_{0.52}$ anode and the NCA880903 cathode was assembled and tested. Note, before cycling, the full cell was activated at 0.05 C for 3 cycles.

Ni-rich Li-ion batteries using the prelithiated anode

The voltage profile and the rate capability of the control NCA880903 cathode//Li cells are shown in Fig. 8a and 8b, respectively. The average specific capacities of half-cell NCA880903 electrode are ∼191, 183, 159, 142, and 112 mAh/g at 0.1 C, 0.2 C, 0.5 C, 1 C, and 2 C, respectively. Notably, a theoretical capacity, C of NCA is about 279 mAh/g [26]. The GCDs of the half-cell prelithiated 3D $rGO_{ae}/Ag_{0.52}$ electrode are shown in Fig. 8a. For the prelithiated 3D $rGO_{ae}/Ag_{0.52}$//NCA full cell, the average specific capacities of prelithiated 3D $rGO_{ae}/Ag_{0.52}$ anode and NCA cathode were used to balance the negative (anode) to positive (cathode) mass ratio. The mass ratio of prelithiated 3D $rGO_{ae}/Ag_{0.52}$ to NCA is 0.22, and the negative capacity to positive capacity ratio (N/P ratio) is 1.22. Fig. 8c shows the GCD profiles at the 1st cycle at different discharge rates. As shown in Fig. 8d, the prelithiated 3D $rGO_{ae}/Ag_{0.52}$//NCA full cell can deliver average capacities of ∼133, 97, 73,

56, 44, and 26 mAh/g (based on the cathode mass) at 0.1 C, 0.25 C, 0.5 C, 0.75 C, 1 C, and 2 C, respectively. The capacity retention was ∼50% after 500 cycles at 1 C (Fig. 8e) which is higher than that of graphene nanosheet//$LiFePO_4$ (14.2% after 40 cycles at 34 mA/g [27, 28], graphene paper//V_2O_5/graphene paper (35.1% after 20 cycles at 10 $\mu A/cm^2$) [28, 29], and prelithiated graphene nanosheet//$LiFePO_4$ (67% after 50 cycles at 34 mA/g) [28, 30]. The energy densities of ∼290, 207, 156, 121, 99, and 63 Wh/kg at power densities of ∼47, 142, 276, 431, 611, and 1265 W/kg, respectively, are achieved based on a total mass of anode and cathode. The voltage of full cell was determined from the voltage profile at 50% of capacities at different discharge rates. The energy density (Fig. 8f) was compared to the VO_2//$LiVOPO_4$ full cell (84 Wh/$kg_{anode+cathode}$) [31], electrospun C/PVDF//electrospun $LiCoO_2$/C/PVDF full cell (144 Wh/$kg_{anode+cathode}$) [32], anatase TiO_2/graphene//$LiFePO_4$ full cell (263 Wh/kg_{anode}) [33], ZnTe-TiO_2-C//LFP@G full cell (242 Wh/$kg_{anode+cathode}$) [34], hard carbon//$LiNi_{0.5}Mn_{1.5}O_4$ (235 Wh/kg $_{anode+cathode}$) [35], hard carbon// $Li_{1.1}Mn_2O_4$ (158 Wh/$kg_{anode+cathode}$) [35], sulfurized carbon//$LiMn_2O_4$ (185 Wh/$kg_{anode+cathode}$) [36], carbon black/silicon/carbon black//$LiCoO_2$/carbon black (200 Wh /$kg_{anode+cathode}$) [37], carbon-coated $Li_4Ti_5O_{12}$ nanowire//$LiMn_2O_4$ (140 Wh/$kg_{anode+cathode}$) [38], anatase TiO_2//$LiNi_{1/3}Mn_{1/3}Co_{1/3}O_2$ (NMC) (120.56 Wh/$kg_{anode+cathode}$) [39], carbon coated porous titanium niobium oxide (TNO@C)//$LiNi_{0.6}Mn_{0.2}O_2$ (NMC) (142.8 Wh/$kg_{anode+cathode}$), and $Li_4Ti_5O_{12}$ (LTO)//$LiNi_{0.8}Co_{0.15}Al_{0.05}O_2$ (NCA) (133 Wh/kg $_{anode+cathode}$) [40]. This result demonstrates that the prelithiated 3D $rGO_{ae}/Ag_{0.52}$ may be an ideal anode for future high-energy density LIBs.

CONCLUSION

In summary, 10-nm AgNPs were successfully synthesized and decorated on the 3D rGO_{ae} supporting material by the polyol synthesis technique. The prelithiation was successfully carried out by a simple direct contact method. The silver content of AgNPs decorated on 3D rGO_{ae} supports was also finely tuned and determined by XPS. The prelithiated anode materials show much higher specific capacity, ICE, and cycling performance as compared to the one without prelithiated. The prelithiated anode of AgNPs decorated on 3D rGO_{ae} with a finely tuned 0.52 at. % Ag having ca. 10 nm in particle diameter exhibits an initial specific capacity of ca. 1580 mAh/g at 0.1 A/g, an ICE of 93% (with 100% for later cycles), and a long cycling stability over 500 cycles. The prelithiated 3D $rGO_{ae}/Ag_{0.52}$//NCA full cell exhibits a high energy density of ∼290 Wh/kg based on total active masses at 0.1 C. The prelithiated anode material in this work may be useful for next-generation batteries.

REFERENCES

1. Song H, Su J, Wang C (2021) Multi-ions electrolyte enabled high performance voltage tailorable room-temperature Ca-metal batteries. *Adv Energy Mater* **11**, ID 2003685.

2. Chi S-S, Wang QR, Han B, Luo C, Jiang YD, Wang J, Wang CY, Yu Y, et al (2020) Lithiophilic Zn sites in porous CuZn alloy induced uniform Li nucleation and dendrite-free Li metal deposition. *Nano Lett* **20**, 2724–2732.

3. Phattharasupakun N, Wutthiprom J, Duangdangchote S, Sawangphruk M (2019) A 3D free-standing lithiophilic silver nanowire aerogel for lithium metal batteries without lithium dendrites and volume expansion: in operando X-ray diffraction. *Chem Commun* **55**, 5689–5692.

4. Huang G, Han JH, Zhang F, Wang ZQ, Kashani H, Watanabe K, Chen MW (2019) Lithiophilic 3D nanoporous nitrogen-doped graphene for dendrite-free and ultrahigh-rate lithium-metal anodes. *Adv Mater* **31**, ID 1970010.

5. Shi HD, Zhang CJ, Lu PF, Dong YF, Wen PC, Wu Z-S (2019) Conducting and lithiophilic MXene/graphene framework for high-capacity, dendrite-free lithium-metal anodes. *ACS Nano* **13**, 14308–14318.

6. Luo L, Chen Z, Ke H, Sha S, Cai G, Li G, Yang H, Yang X, et al (2019) Facile synthesis of three-dimensional $MgFe_2O_4$/graphene aerogel composites for high lithium storage performance and its application in full cell. *Mater Des* **182**, ID108043.

7. Atar N, Eren T, Yola ML (2015) Ultrahigh capacity anode material for lithium ion battery based on rod gold nanoparticles decorated reduced graphene oxide. *Thin Solid Films* **590**, 156–162.

8. Yang C, Yao Y, He S, Xie H, Hitz E, Hu L (2017) Ultrafine silver aanoparticles for seeded lithium deposition toward stable lithium metal anode. *Adv Mater* **29**, ID 1702714.

9. Lee Y-G, Fujiki S, Jung C, Suzuki N, Yashiro N, Omoda R, Ko D-S, Shiratsuchi T, et al (2020) High-energy long-cycling all-solid-state lithium metal batteries enabled by silver-carbon composite anodes. *Nat Energy* **5**, 299–308.

10. Shi L, Wang W, Wang A, Yuan K, Jin Z, Yang Y (2015) Si nanoparticles adhering to a nitrogen-rich porous carbon framework and its application as a lithiumion battery anode material. *J Mater Chem A* **3**, 18190–18197.

11. Jung H-R, Lee W-J (2011) Ag/poly(3,4-ethylenedi-oxythiophene) nanocomposites as anode materials for lithium ion battery. *Solid State Ion* **187**, 50–57.

12. Sroysee W, Suktha P, Kongsawatvoragul K, Vadivel S, Sawangphruk M (2020) Graphene aerogels with ultrahigh pore volume for organic dye adsorption and high-energy lithium batteries. *Ind Eng Chem Res* **59**, 20719–20729.

13. Chiochan P, Kosasang S, Ma N, Duangdangchote S, Suktha P, Sawangphruk M (2020) Confining Li_2S_6 catholyte in 3D graphene sponge with ultrahigh total pore volume and oxygen-containing groups for lithium-sulfur batteries. *Carbon* **158**, 244–255.

14. Biasi LD, Schwarz B, Brezesinski T, Hartmann P, Janek J, Ehrenberg H (2019) Chemical, structural, and electronic aspects of formation and degradation behavior on different length scales of Ni-rich NCM and Li-rich HE-NCM cathode materials in Li-ion batteries. *Adv Mater* **31**, ID 1900985.

15. Phattharasupakun N, Wutthiprom J, Duangdangchote S, Sarawutanukul S, Tomon C, Duriyasart F, Tubtimkuna S, Aphirakaramwong C, et al (2021) Core-shell Ni-rich NMC-Nanocarbon cathode from scalable solvent-free mechanofusion for high-performance 18650 Li-ion batteries. *Energy Storage Mater* **36**, 485–495.

16. Wutthiprom J, Phattharasupakun N, Tomon C, Sawangphruk M (2020) Scalable solvent-free mechanofusion and magnesiothermic reduction processes for obtaining carbon nanospheres-encapsulated crystalline silicon anode for Li-ion batteries. *Electrochim Acta* **352**, ID 136457.

17. Sawangphruk M, Srimuk P, Chiochan P, Krittayavathananon A, Luanwuthi S, Limtrakul J (2013) High-performance supercapacitor of manganese oxide/reduced graphene oxide nanocomposite coated on flexible carbon fiber paper. *Carbon* **60**, 109–116.

18. Rajoba SJ, Sartale SD, Jadhav LD (2018) Investigating functional groups in GO and r-GO through spectroscopic tools and effect on optical properties. *Optik* **175**, 312–318.

19. Shan H, Xiong D, Li X, Sun Y, Yan B, Li D, Lawes S, Cui Y, et al (2016) Tailored lithium storage performance of graphene aerogel anodes with controlled surface defects for lithium-ion batteries. *Appl Surf Sci* **364**, 651–659.

20. Shen W, Wang X, Ge Y, Feng H, Feng L (2019) Synthesis and characterization of AgO/g-C_3N_4 hybrids with enhanced visible-light photocatalytic activity for Rhodamine B degradation and bactericidal inactivation. *Colloids Surf A: Physicochem Eng Asp* **575**, 102–110.

21. Sui Z-Y, Meng Q-H, Li J-T, Zhu J-H, Cui Y, Han B-H (2014) High surface area porous carbons produced by steam activation of graphene aerogels. *J Mater Chem A* **2**, 9891–9898.

22. Iamprasertkun P, Krittayavathananon A, Sawangphruk M (2016) N-doped reduced graphene oxide aerogel coated on carboxyl-modified carbon fiber paper for high-performance ionic-liquid supercapacitors. *Carbon* **102**, 455–461.

23. Zhang Y, Zong X, Zhan L, Yu X, Gao J, Xun C, Li P, Wang Y (2018) Double-shelled hollow carbon sphere with microporous outer shell towards high performance lithium-sulfur battery. *Electrochim Acta* **284**, 89–97.

24. Thielemans W, Warbey CR, Walsh DA (2009) Permselective nanostructured membranes based on cellulose nanowhiskers. *Green Chem* **11**, 531–537.

25. Sawangphruk M, Foord JS (2010) Permselective properties of polystyrene opal films at diamond electrode surfaces. *Phys Chem Chem Phys* **12**, 7856–7864.

26. Purwanto A, Yudha CS, Ubaidillah U, Widiyandari H, Ogi T, Haerudin H (2018) NCA cathode material: synthesis methods and performance enhancement efforts. *Mater Res Express* **5**, ID 122001.

27. Vargas Ó, Caballero Á, Morales J (2015) Deficiencies of chemically reduced graphene as electrode in full Li-ion cells. *Electrochim Acta* **165**, 365–371.

28. Huang Y, Li K, Yang G, Aboud MFA, Shakir I, Xu Y (2018) Ultrathin nitrogen-doped carbon layer uniformly supported on graphene frameworks as ultrahigh-capacity anode for lithium-ion full battery. *Small* **14**, ID 1703969.

29. Gwon H, Kim H-S, Lee KU, Seo D-H, Park YC, Lee YS, Ahn BT, Kang K (2011) Flexible energy storage devices based on graphene paper. *Energy Environ Sci* **4**, 1277–1283.

30. Vargas O, Caballero A, Morales J, Rodríguez-Castellón E (2014) Contribution to the understanding of capacity fading in graphene nanosheets acting as an anode in full Li-ion batteries. *ACS Appl Mater Interfaces* **6**, 3290–3298.

31. Shao M, Deng J, Zhong F, Cao Y, Ai X, Qian J, Yang H (2019) An all-vanadium aqueous lithium ion battery with high energy density and long lifespan. *Energy Storage Mater* **18**, 92–99.

32. Self EC, McRen EC, Wycisk R, Pintauro PN (2016) $LiCoO_2$-based fiber cathodes for electrospun full cell Li-ion batteries. *Electrochim Acta* **214**, 139–146.

33. Choi D, Wang D, Viswanathan VV, Bae IT, Wang W, Nie Z, Zhang J-G, Graff GL, et al (2010) Li-ion batteries from $LiFePO_4$ cathode and anatase/graphene composite anode for stationary energy storage. *Electrochem Commun* **12**, 378–381.

34. Nguyen QH, Nguyen QH, Hur J (2020) High-performance $ZnTe$-TiO_2-C nanocomposite with half-cell and full-cell applications as promising anode material for Li-ion batteries. *Appl Surf Sci* **509**, ID 144718.

35. Yu H, Dong X, Pang Y, Wang Y, Xia Y (2017) High power lithium-ion battery based on spinel cathode and hard carbon anode. *Electrochim Acta* **228**, 251–258.

36. Berhe GB, Su W-N, Huang C-J, Hagos TM, Hagos TT, Bezabh HK, Weret MA, Abrha LH, et al (2019) A new class of lithium-ion battery using sulfurized carbon anode from polyacrylonitrile and lithium manganese oxide cathode. *J Power Sources* **434**, ID 126641.

37. Li C, Shi T, Yoshitake H, Wang H (2017) A flexible high-energy lithium-ion battery with a carbon black-sandwiched Si anode. *Electrochim Acta* **225**, 11–18.

38. Su X, Liu J, Zhang C, Huang T, Wang Y, Yu A (2016) High power lithium-ion battery based on a $LiMn_2O_4$ nanorod cathode and a carbon-coated $Li_4Ti_5O_{12}$ nanowire anode. *RSC Adv* **6**, 107355–107363.

39. Moretti A, Kim G-T, Bresser D, Renger K, Paillard E, Marassi R, Winter M, Passerini S (2013) Investigation of different binding agents for nanocrystalline anatase TiO_2 anodes and its application in a novel, green lithium-ion battery. *J Power Sources* **221**, 419–426.

40. Fang Z, Peng J, Ma N, Liang L, Gao H, Zhou H, Jin X, Yang J, et al (2018) Preparation and pptimization of new high-power nanoscale $Li_4Ti_5O_{12}$ full-cell system. *J Nanosci Nanotechnol* **18**, 8232–8239.